High-energy anomaly in Nd_{2-x}Ce_{x}CuO_{4} investigated by angle-resolved photoemission spectroscopy and quantum Monte Carlo simulations

F. Schmitt, B. Moritz, S. Johnston, S.-K. Mo, M. Hashimoto, R. G. Moore, D.-H. Lu, E. Motoyama, M. Greven, T. P. Devereaux, and Z.-X. Shen

Phys. Rev. B **83**, 195123 — Published 13 May 2011

DOI: 10.1103/PhysRevB.83.195123

High-energy anomaly in NCCO investigated by ARPES and quantum Monte Carlo simulations

F. Schmitt[1,2], B. Moritz[2,3], S. Johnston[2,4,5], S.-K. Mo[6], M. Hashimoto[1,2,6], R. G. Moore[7], D.-H. Lu[7], E. Motoyama[8], M. Greven[9], T. P. Devereaux[2,8], and Z.-X. Shen[1,2,7,8]
[1]*Department of Applied Physics, Via Pueblo Mall, Stanford University, Stanford, CA 94305, USA*
[2]*Stanford Institute for Materials and Energy Science, SLAC National Accelerator Laboratory, Menlo Park, CA 94025, USA*
[3]*Department of Physics and Astrophysics, University of North Dakota, Grand Forks, ND 58202, USA*
[4]*Department of Physics and Astronomy, University of Waterloo, Waterloo, Ontario N2L 3G1, Canada*
[5]*Institute for Solid State Research, IFW Dresden, P.O. Box 27 01 16, D-01171 Dresden, Germany*
[6]*Advanced Light Source, Lawrence Berkeley National Laboratory, Berkeley, California 94720, USA*
[7]*Stanford Synchrotron Radiation Lightsource, 2575 Sand Hill Road, Menlo Park, CA 94025, USA*
[8]*Geballe Laboratory for Advanced Materials, 476 Lomita Mall, Stanford University, Stanford, CA 94305, USA and*
[9]*School of Physics & Astronomy, University of Minnesota, MN 55455, USA*

Recent high binding-energy angle-resolved photoemission spectroscopy (ARPES) experiments reveal a change in band dispersion in the high-temperature superconducting cuprates (HTSCs) known as the high-energy anomaly (HEA). Despite considerable experimental and theoretical attention, the origin of the HEA remains a topic of some controversy. In this paper we present systematic and comprehensive experimental evidence on the origin of the HEA from ARPES measurements on the electron-doped HTSC material $Nd_{2-x}Ce_xCuO_4$ at a number of dopings across the phase diagram and over the entire Brillouin zone (BZ). Comparing these new experimental findings to quantum Monte Carlo simulations of the single-band Hubbard model across the BZ and for various dopings demonstrates that this simple model qualitatively reproduces the key experimental features of the HEA and points to significant self-energy and band renormalization effects accompanying strong electron correlations as its origin rather than coupling to any one emergent bosonic mode, *e.g.* antiferromagnetic spin fluctuations. We conclude from comparison to this simple model that the HEA in these systems should be regarded as a crossover from a coherent quasiparticle band at low binding-energies, emergent from the upper Hubbard band in electron-doped HTSCs due to doping and modified by subsequent strong band renormalization effects, to oxygen valence bands at higher binding-energy that would be revealed in simulations explicitly incorporating these important orbital degrees of freedom.

I. INTRODUCTION

Angle-resolved photoemission spectroscopy (ARPES), a technique based on the photoelectric effect, provides direct experimental access to the single-particle spectral function $A(\mathbf{k}, \omega)$.[1] This technique is especially well suited for the study of two-dimensional and quasi-two-dimensional materials, like the high-temperature superconducting cuprates (HTSCs),[2] since the electron/photoelectron momentum is conserved parallel to the sample surface.[1] The HTSC materials become superconducting upon either hole or electron doping the insulating parent compounds and are noted for their high superconducting T_C on the p-doped side. However, the mechanism that gives rise to their superconductivity remains a topic of considerable debate despite extensive study since their initial discovery. ARPES has provided valuable insight on universal features in the cuprate bandstructure within a few 100 meV of the Fermi level[1,3,4] that has informed our current understanding of the important degrees of freedom and relevant low energy physics in these systems.

In recent years, ARPES experiments on HTSCs have been extended to regions of high binding-energy $\sim 0.5 - 1.0$ eV.[5–19] ARPES reveals dispersing quasiparticles with sharp spectral features close to E_F that give way to an almost vertical dispersion around ~ 0.3 eV for the hole(h)-doped HTSCs[6–14,16,18], and ~ 0.5 eV for the electron(e)-doped HTSCs.[6,15,17–19] This vertical dispersion or "waterfall" eventually merges with the incoherent valence bands at higher binding-energies. This crossover, termed the high-energy anomaly (HEA), appears at different energies in experiments on either hole(h)- or electron(e)-doped families, highlighting an electron-hole doping asymmetry.

Most experimental studies focused on the HEA have been conducted on h-doped HTSCs.[6–14,16,18] In some of these early studies, the HEA was tied to a presumed underlying dispersion through a sizable renormalization in the quasiparticle bare band.[9,12,13] Density functional theory results, based on the local density approximation (LDA) fit to the entire band structure including the HEA, yield a band bottom $\sim 1.2 - 1.5$ eV.[9] These findings led to several scenarios for the emergence of the HEA based on interaction with high energy bosonic degrees of freedom,[12,13,20–23] chiefly antiferromagnetic spin fluctuations or paramagnons,[12,21–23] adding to the growing list of scenarios for the emergence of this feature in the band dispersion.[8–11,14,24–29] However, the vertical drop-off at higher energies, and apparent "back-bending" in some data, calls into question this large bandwidth, quasiparticle scenario and the justification for LDA fits or even Lorentzian momentum distribution curve (MDC) fits in the energy window below the HEA energy scale, also highlighted by the results from laser-based ARPES.[16]

While this topic has been studied rather extensively for h-doped materials, there is far less work concerning e-doped systems.[6,15,17–19] Ikeda *et al.*[17] extracted the onset energy as a function of position in the Brillouin zone (BZ) for $Nd_{2-x}Ce_xCuO_4$ (NCCO) with $x = 0.15$. Compared to the HEA in $La_{2-x}Sr_xCuO_4$ (LSCO), where analysis[10] of $x = 0.17$ samples revealed a BZ-dependence that resembles the superconducting gap profile, Ikeda *et al.*[17] found similar behavior, but at a higher energy attributed to a chemical potential shift between the h- and e-doped materials. Although spin fluctuations or paramagnons exhibit the correct energy scale for h-doped materials, coupling to these modes would not account for this difference in energy scale between h- and e-doped HTSCs as observed in this limited number of experiments. This sparsity of results makes statements about the universality of the HEA, or even its origin, an extrapolation or expectation not directly verified by experiment. The results presented in this work bridge that gap by providing complementary data about e-doped materials at low (4%), intermediate (11%), and high (17%) doping levels as a function of both energy and momentum throughout the BZ.

Previous quantum Monte Carlo (QMC) work concentrating on band structure differences throughout the BZ for optimal, or near optimal, h- and e-doping,[18,30] and other work based on a cluster extension of dynamical mean field theory (DMFT) concentrating on momentum and doping dependence[31] indicated that the key features of the HEA can be captured by the strongly correlated, single-band Hubbard model through a substantial renormalization of the underlying bandsturcture due to strong electron-electron correlations that give rise to a coherent, shallow quasiparticle band (QPB) at low binding energy in these systems. The relevant Mott-Hubbard physics captured by this model already is believed to be substantially universal in the HTSCs providing an effective low energy theory.[32–35] While the HEA appears to be universal, there are reports of strong matrix element effects[11,14] that add complexity in the data analysis. However, previous comparative analysis demonstrates that the HEA should not be attributed solely to matrix element effects[11,14] or weak coupling to bosonic degrees of freedom, especially antiferromagnetic spin fluctuations or paramagnons, as highlighted in the work employing cluster DMFT.[31] In the present study, systematic data on NCCO and additional evidence from simulations elucidate the momentum and doping dependence of the HEA, reinforcing previous conclusions: the HEA represents a crossover of spectral intensity from the coherent QPB at low binding-energy to oxygen valence bands at higher binding-energy. We find that the energy position of the HEA tracks the position of this QPB bottom; therefore, we claim that this band bottom – observed from close to the BZ center out to $(\pi, 0)$ – represents the physically relevant measure of the HEA energy scale.

II. EXPERIMENTAL METHODS

ARPES data were taken at beamline 5-4 of the Stanford Synchrotron Radiation Lightsource (SSRL) at the SLAC National Accelerator Laboratory with Scienta SES200 and R4000 analyzers, and at beamline 10.0.1 of the Advanced Light Source (ALS) at the Lawrence Berkeley National Laboratory with a Scienta R4000 analyzer. At SSRL, the a-(b-)axis was aligned at 45° to the incident p-polarized light for the nodal cuts along (0, 0) - (π, π), and parallel to the incident p-polarized light for the cuts along (0, 0) - (π, 0). The energy resolution was $\sim$ 10 meV with an angular resolution $\sim$ 0.3°. At ALS, the incident light was s-polarized at grazing incidence with the polarization parallel to the crystal a-(b-)axis. The energy resolution was set to $\sim$ 15 meV, with an angular resolution $\sim$ 0.3°. Unless otherwise specified, the incident photons had an energy of 16.75 eV at SSRL and 53 eV at ALS. All samples were cleaved in situ at pressures better than 4×10^{-11} torr and the measurement temperature was 10 K, unless otherwise specified. Single crystals of NCCO were grown at Stanford University as described in Ref. 36. The doping level was determined by inductively coupled plasma spectroscopy[36] with an error of $\pm$0.7% Ce.

III. RESULTS

Fig. 1(a) shows the spectral function of NCCO ($x = 17\%$) along an unsymmetrized cut through the BZ diagonal from ($-\pi/a$, $-\pi/a$) to (π/a, π/a). One finds a band dispersion with finite band velocity between E_F and $\sim$ 0.4 eV along with sharpened spectral features approaching E_F. Moving to higher binding energies $>$ 0.5 eV, the band dispersion becomes vertical and the intensity decreases around 0.5 eV. The dispersion remains vertical with an increasing linewidth until the features merge with the valence band at $\sim$ 1.5 eV. A reduction in intensity can be seen in both the energy distribution curves (EDCs) (Fig. 1(b)) and MDCs (Fig. 1(c)) at approximately the same energy scale (0.5 eV); the MDCs appear to show a back-bending and deep dispersion moving toward higher binding-energies while the EDCs show a shallow band, albeit with a reduced intensity approaching the BZ center. This behavior should be compared to that observed in similar comparisons between EDC and MDC derived dispersion for the h-doped materials.[7,8] As a guide to the eye, the band's second derivative extracted from maxima of the EDC and MDC lineshapes has been overlaid in Figs. 1(b) and (c), highlighting the change at $\sim$ 0.5 eV. While the error in the EDC fit grows rapidly with decreasing intensity, and should therefore be viewed with a degree of caution, the data still show a remnant of the shallow band beyond the momentum space position characterizing the HEA from the MDC fits. This point will be discussed in greater detail below.

Having established the energy scale of the HEA in the nodal region, we now turn to the momentum dependence in the entire BZ. Fig. 2 shows isoenergy cuts through the first and second BZ of $x = 4\%$ NCCO measured at a photon energy of 53 eV. The data clearly show that matrix element effects suppress intensity in the first BZ relative to that in the second BZ. At E_F only the antinodal points (π/a, 0), and those equivalent by symmetry, possess significant intensity, with the nodal part of the Fermi surface eventually becoming visible at dopings greater than $\sim$ 15%.[37,38] These isoenergy surfaces closely resemble those from Pb-doped $Bi_2Sr_2CaCu_2O_{8+\delta}$ (Pb-Bi2212), an h-doped HTSC:[7] with increasing binding energy, the isoenergy surfaces evolve from hole-like "circles" centered around (π/a, π/a) to electron-like "diamonds" centered around the BZ center. In contrast to the Bi compound, almost the entire Fermi circle is visible in the data for NCCO, except for the hot spots in the vicinity of the antiferromagnetic BZ boundary, as discussed elsewhere.[38–40]

Despite specific differences, such as the HEA energy scale, the general evolution with increasing binding-energy appears strikingly similar between h- and e-doped compounds. The isoenergy surfaces shrink to a diamond approaching 0.5 eV (0.3 eV for h-doped) binding energy whose position and general shape appear to "lock-in" for energies greater than 0.5 eV (0.3 eV for h-doped). The shape of the isoenergy surfaces do begin to deviate from the diamond-like form with continued increase in the binding-energy which can be attributed to matrix element effects. Since the intensity scale for each isoenergy cut in Fig. 2 has been normalized independently, the significant reduction in intensity at binding-energies above the HEA energy scale, like that shown in Fig. 1 is not visible here. Similar to Pb-Bi2212, the diamond-like shape of the isoenergy surface aligns roughly with lines connecting (0, $\pi/2a$) and ($\pi/2a$, 0), and other symmetry equivalent points within the first BZ. This behavior also has been observed by Ikeda *et al.*[17] in NCCO (x=15%) and by Chang *et al.*[10] in LSCO (x=17%) — both near optimal doping — indicating the possibility that this is a universal feature in the HTSCs. We note that the dopings we measured (4%, 11%, 15%(not shown), and 17%) cross from the antiferromagnetic (AF) insulating phase to well into the superconducting phase where the long-range AF ordering no longer exists[41], while the HEA feature itself (i.e. the energy and position) does not change appreciably in the measured doping range. Therefore, AF long-range order alone seems not to capture the HEA.

Fig. 3 shows the photoemission intensity along high-symmetry cuts as a function of energy and BZ position starting from $(0, 0)$ moving along the BZ axis to (π/a, 0) (left panel), along the BZ boundary to (π/a, π/a) (middle panel), and finally back to $(0, 0)$ (right panel). The right panel with the familiar nodal cut clearly shows the HEA; in the

middle panel the band bottom along the antinodal cut can be seen at ~ 0.3 eV; in the left panel along the BZ axis from (π/a, 0) to $(0,0)$, one still sees the remnants of the band bottom, albeit with a very weak intensity near (π/a, 0) due to matrix element effects. The isointensity contours appearing in the figure stress the band dispersion. The isointensity contours and EDCs curves, shown in the lower panels of Fig. 3, enable an estimation of the band bottom throughout the BZ, especially along those cuts approaching the BZ center along the BZ axis and diagonal. A slight increase of intensity over a very broad energy range at ~ 0.5 eV binding-energy suggests that the almost dispersionless QPB extends from (π/a, 0) to (0, 0) (Fig. 3, left panel) with a slight dip to higher binding energies around ($\pi/2a$, 0). Similarly for the nodal cut (Fig. 3, right panel), two branches appear in the derived dispersion: a branch that drops-off in a nearly vertical "waterfall", typically associated with the HEA, and a shallow, almost dispersionless, branch at $\sim$ 0.5 eV binding-energy, with a large linewidth and faint intensity approaching the BZ center. This is reminiscent of the branching observed by Graf *et al.* in Bi2201, Bi2212, Pb-Bi2212, and Eu-LSCO.[7,8] In NCCO this branching, although weak, appears robustly in nodal cuts, especially for photon energies ~ 18 eV (not shown).

These findings prompt a closer look at how the band bottom disperses from the antinodal region toward the BZ center. Fig. 4 displays cuts taken parallel to the crystal a-(b-)axis, with the cut locations indicated in Fig. 4 (a). Following the cuts from the antinodal region to the BZ center (Fig. 4 (b)-(h)), a band bottom can be clearly discerned more than half-way toward the BZ center (Fig. 4 (b)-(f)). It is difficult to discern the band bottom from the cut in Fig. 4 (g); in Fig. 4 (h), the isointensity contours and the band remnants near the edges of the panel suggest a maximum intensity at ~ 0.4 eV. This is corroborated by looking at the EDC band maxima along $(0,0)$ - (π/a, 0) (cf. Fig. 3).

Recent QMC and cluster DMFT simulations[18,30,31] of the single-band Hubbard model show a momentum-space or BZ dependence to the HEA in e-doped materials similar to that shown here or in Ref. 17. Similarly, there was also decent agreement between these simulations and results from experiments on h-doped systems.[7–9,16] Fig. 5 displays the momentum dependence of the QMC simulated band dispersion for a sequence of cuts like those shown in Fig. 4. The simulations of the single-band Hubbard model have been performed with $t = 400$ meV and $U = 8t = 3.2$ eV; further details can be found in Refs. 18 and 30 and references therein. By comparing Figs. 4 and 5, one can follow the band dispersion develop all the way from the antinodal region to the BZ center: Near the antinodal region, a parabolic dispersion with a band bottom at around 300 meV in the antinodal region is observed. The band bottom continually increases in binding energy to about 500 meV and becomes fainter and fainter towards the BZ center. The overall behavior like the dispersion, fading, and intensity distribution within each cut agree well between simulated and measured data.

To understand the doping evolution of these features, we proceed by extracting EDC band bottoms for NCCO with $x = 4\%, 11\%$, and 17% for momentum-space points along the $(0,0)$ to (π/a, 0) direction in the first and second BZ, respectively. The resulting EDCs are displayed in Fig. 6. Starting at the antinode, there is a clear band bottom. Moving toward the BZ center, the intensity decreases as the linewidth becomes increasingly broad. It appears that a feature at ~ 0.5 eV binding-energy can only be seen at the BZ center for 11% and 17% doping in the first BZ (Fig. 6 (c), (e)). In the second BZ, the band disperses downward toward higher binding-energies $\sim 0.5 - 0.7$ eV and the band intensity fades at $\sim 0.3\ \pi/a$. We show EDCs from QMC simulations at $n = 1.05(5\%)$, $n = 1.15(15\%)$, and $n = 1.20(20\%)$ electron filling (electron doping) in Fig. 7. Again, a quantitative analysis could be made with a suitable choice of the QMC simulation energy scale ($t \sim 400$ meV), but the main purpose of these figures is for a qualitative comparison to the experimental results presented in this work. The figure shows EDCs along both the BZ axis in panels (a), (b), and (c) and the BZ diagonal in panels (d), (e), and (f). The intensity of the EDC curves near the BZ center increases with increasing electron filling (lowest curve in each panel). Moving from either the antinode or node toward the BZ zone center, it becomes easier to track the EDC-derived band closer to the BZ center with increasing electron filling (note the progression from panels (a) to (c) or (d) to (f)) in agreement with results shown in Fig. 6. The derived energy scale for either the band bottom or HEA does change with changes to the electron filling in apparent contrast to the experimental determination; however, the single-band Hubbard model is only a low energy effective theory and this behavior also has been seen in cluster DMFT simulations on the h-doped side of the phase diagram.[31] The single-band Hubbard model qualitatively captures much of the universal behavior in these systems and is primarily valid near half-filling and in a restricted portion of the BZ near the AF zone boundary. A more quantitative comparison would come from explicit consideration of the multiorbital character of the bands in those compounds with a treatment of strong correlations. This can be achieved for example with density functional theory plus DMFT[29] or by using tight-binding derived multiband/multiorbital Hubbard models[42] which can explicitly capture the copper and oxygen content of the valence bands throughout the BZ and over a range of energies.

Figure 8 shows the band bottoms extracted from EDCs along the BZ axis for the three different dopings (4%, 11%, and 17%) in both the first and second BZ. Since the EDC linewidth is rather broad and the band possesses a relatively low intensity, plotting the maximum of the EDC second derivative is a more robust and less model-dependent method than fitting to a Lorentzian lineshape with a large background. The major drawbacks are a loss of information pertaining to the EDC linewidth and the relative error in position. However, from the EDC linewidths in Fig. 4, we

estimate the error to be approximately ±50 meV which increases approaching the BZ center. At the BZ boundary, the extracted band bottom is ∼ 0.3 eV for 17% doping, and decreases with decreasing doping, as expected. Up to halfway toward the BZ center, the band bottom exhibits the same BZ dependence as the HEA extracted and plotted by Ikeda *et al.*,[17] similar to the feature observed by Chang *et al.*[10] The HEA occurs in close proximity to the band bottom in the antinodal region, but near the BZ center, the HEA appears to display its characteristic "waterfall" at a different position than the extracted band bottom.

At $\sim 0.5\pi/a$ there seems to be a fork in the dispersion. On one hand, the band continues to disperse downward toward the BZ center with the intensity decreasing to background levels prior to reaching $(0, 0)$. On the other hand, a very faint, broad, and dispersionless band emerges, at ∼ 0.4 eV binding-energy, approaching the BZ center. These two features resemble what has been seen in Bi2212[9] near the BZ center, where a large, trough-like dispersion was found together with a valence band at a maximum binding-energy ∼ 1 eV, in agreement with results from LDA calculations. Nevertheless, the energy scales between h- and e-doped HEA are noticeably different, and we also note that while there seem to be two structures visible in Fig. 4, none of the data display both features simultaneously, potentially due to their weak intensity. From QMC simulations,[18,30] we believe that the latter, dispersionless feature is actually a remnant of the QPB and its faintness likely stems from matrix element effects.[18,23] The dichotomy in energy scales originates from the presence of the charge-transfer gap — or Mott gap in the case of the single-band Hubbard QMC simulations done here — located on the unoccupied or occupied side of the Fermi level. The cross-over takes place primarily within the Zhang-Rice singlet (or lower Hubbard band) for h-doped compounds and across the charge-transfer (or Mott) gap in e-doped systems, respectively.

IV. SUMMARY AND CONCLUSIONS

In summary, we have presented systematic experimental photoemission data on NCCO for various dopings and compared them with QMC simulations of the single-band Hubbard model. There is good, qualitative agreement between the experimental results and simulations throughout the BZ and for different doping levels in the energies and positions of prominent features associated with the HEA. Increased doping causes a downward shift in the derived band bottom in the antinodal region of about 100 meV between 4% and 17% doping (cf. Fig. 4 or Fig. 8), but this becomes obscured approaching the BZ center, giving a rather universal HEA energy scale for e-doped materials, similar to but different from their h-doped counterparts.[9]

Based on comparison to QMC simulations, we speculate that the actual band bottom is the faint, dispersionless feature at ∼ 0.5 eV binding energy that appears near the BZ center and is a remnant of the dispersive QPB found near the node and antinode. Furthermore, we identify the HEA with a crossover between the band bottom of the QPB and the incoherent valence band resulting from a combination of strong correlations, transfer of spectral weight, and matrix element effects. While tuning the single-band Hubbard model parameters may make the qualitative agreement between experiment and theory more quantitative, a robust quantitative comparison throughout the BZ and over a wide energy range requires the use of multiorbital models that can explicitly capture the changing orbital character of bands in different regions, especially with regard to the evolution in the vicinity of the HEA cross-over.

ACKNOWLEDGMENTS

We thank C. Kim and W.-S. Lee for valuable discussions. This work was supported in part by the Department of Energy, Office of Basic Energy Sciences, Division of Materials Sciences and Engineering, under contract DE-AC02-76-SFO0515. The crystal growth work was supported by the afore-mentioned contract and by the NSF under Grant No. DMR-0705086. SJ would like to acknowledge financial support from Natural Sciences and Engineering Research Council of Canada and Foundation for Fundamental Research on Matter. Portions of this research were carried out at the Stanford Synchrotron Radiation Lightsource, a national user facility operated by Stanford University on behalf of the U.S. Department of Energy, Office of Basic Energy Sciences. The Advanced Light Source is supported by the Director, Office of Science, Office of Basic Energy Sciences, of the U.S. Department of Energy under Contract No. DE-AC02-05CH11231. Computational results were made possible in part by the resources of the National Energy Research Scientific Computing Center, which is supported by the Office of Science of the U.S. Department of Energy under Contract No. DE-AC02-05CH11231. Three of the authors (BM, SJ, TPD) wish to thank the Walther-Meißner-Institut for their hospitality during part of this work.

[1] A. Damascelli, Z. Hussain, and Z.-X. Shen, Rev. Mod. Phys. **75**, 473 (2003).
[2] J. G. Bednorz and K. A. Müller, Z. Phys. B **64**, 189 (1986).
[3] X. J. Zhou, T. Cuk, T. P. Devereaux, N. Nagaosa, and Z.-X. Shen, in *Handbook of High-Temperature Superconductivity: Theory and Experiment*, edited by J. R. Schrieffer and J. S. Brooks (Springer-Verlag, New York, 2007).
[4] N. P. Armitage, P. Fournier, and R. L. Greene, Rev. Mod. Phys. **82**, 2421 (2010).
[5] F. Ronning, K. M. Shen, N. P. Armitage, A. Damascelli, D. H. Lu, Z.-X. Shen, L. L. Miller, and C. Kim, Phys. Rev. B **71**, 094518 (2005).
[6] Z. H. Pan, P. Richard, A. V. Fedorov, T. Kondo, T. Takeuchi, S. L. Li, P. Dai, G. D. Gu, W. Ku, Z. Wang, and H. Ding, arXiv:cond-mat/0610442 [cond-mat.supr-con] (2006).
[7] J. Graf, G.-H. Gweon, K. McElroy, S. Y. Zhou, C. Jozwiak, E. Rotenberg, A. Bill, T. Sasagawa, H. Eisaki, S. Uchida, H. Takagi, D.-H. Lee, and A. Lanzara, Phys. Rev. Lett. **98**, 067004 (2007).
[8] J. Graf, G.-H. Gweon, and A. Lanzara, Physica C **460-462**, 194 (2007).
[9] W. Meevasana, X. J. Zhou, S. Sahrakorpi, W. S. Lee, W. L. Yang, K. Tanaka, N. Mannella, T. Yoshida, D. H. Lu, Y. L. Chen, R. H. He, H. Lin, S. Komiya, Y. Ando, F. Zhou, W. X. Ti, J. W. Xiong, Z. X. Zhao, T. Sasagawa, T. Kakeshita, K. Fujita, S. Uchida, H. Eisaki, A. Fujimori, Z. Hussain, R. S. Markiewicz, A. Bansil, N. Nagaosa, J. Zaanen, T. P. Devereaux, and Z.-X. Shen, Phys. Rev. B **75**, 174506 (2007).
[10] J. Chang, S. Pailhés, M. Shi, M. Månsson, T. Claesson, O. Tjernberg, J. Voigt, V. Perez, L. Patthey, N. Momono, M. Oda, M. Ido, A. Schnyder, C. Mudry, and J. Mesot, Phys. Rev. B **75**, 224508 (2007).
[11] D. S. Inosov, J. Fink, A. A. Kordyuk, S. V. Borisenko, V. B. Zabolotnyy, R. Schuster, M. Knupfer, B. Büchner, R. Follath, H. A. Dürr, W. Eberhardt, V. Hinkov, B. Keimer, and H. Berger, Phys. Rev. Lett. **99**, 237002 (2007).
[12] T. Valla, T. E. Kidd, W.-G. Yin, G. D. Gu, P. D. Johnson, Z.-H. Pan, and A. V. Fedorov, Phys. Rev. Lett. **98**, 167003 (2007).
[13] B. P. Xie, K. Yang, D. W. Shen, J. F. Zhao, H. W. Ou, J. Wei, S. Y. Gu, M. Arita, S. Qiao, H. Namatame, M. Taniguchi, N. Kaneko, H. Eisaki, K. D. Tsuei, C. M. Cheng, I. Vobornik, J. Fujii, G. Rossi, Z. Q. Yang, and D. L. Feng, Phys. Rev. Lett. **98**, 147001 (2007).
[14] D. S. Inosov, R. Schuster, A. A. Kordyuk, J. Fink, S. V. Borisenko, V. B. Zabolotnyy, D. V. Evtushinsky, M. Knupfer, B. Büchner, R. Follath, and H. Berger, Phys. Rev. B **77**, 212504 (2008).
[15] S. R. Park, C. S. Leem, Y. S. Roh, K. J. Choi, J. H. Kim, B. J. Kim, H. Koh, H. Eisaki, D. H. Lu, Z.-X. Shen, N. Armitage, and C. Kim, J. Phys. Chem. Sol. **69**, 2939 (2008).
[16] W. Zhang, G. Liu, J. Meng, L. Zhao, H. Liu, X. Dong, W. Lu, J. S. Wen, Z. J. Xu, G. D. Gu, T. Sasagawa, G. Wang, Y. Zhu, H. Zhang, Y. Zhou, X. Wang, Z. Zhao, C. Chen, Z. Xu, and X. J. Zhou, Phys. Rev. Lett. **101**, 017002 (2008).
[17] M. Ikeda, T. Yoshida, A. Fujimori, M. Kubota, K. Ono, Y. Kaga, T. Sasagawa, and H. Takagi, Phys. Rev. B **80**, 184506 (2009).
[18] B. Moritz, F. Schmitt, W. Meevasana, S. Johnston, E. M. Motoyama, M. Greven, D. H. Lu, C. Kim, R. T. Scalettar, Z.-X. Shen, and T. P. Devereaux, New Journal of Physics **11**, 093020 (2009).
[19] A. F. Santander-Syro, T. Kondo, J. Chang, A. Kaminski, S. Pailhés, M. Shi, L. Patthey, A. Zimmers, B. Liang, P. Li, and R. L. Greene, arXiv:0903.3413v1 [cond-mat.supr-con] (2009).
[20] R. S. Markiewicz and A. Bansil, Phys. Rev. B **75**, 020508 (2007).
[21] A. Macridin, M. Jarrell, T. Maier, and D. J. Scalapino, Phys. Rev. Lett. **99**, 237001 (2007).
[22] R. S. Markiewicz, S. Sahrakorpi, and A. Bansil, Phys. Rev. B **76**, 174514 (2007).
[23] S. Basak, T. Das, H. Lin, J. Nieminen, M. Lindroos, R. S. Markiewicz, and A. Bansil, Phys. Rev. B **80**, 214520 (2009).
[24] E. Manousakis, Phys. Rev. B **75**, 035106 (2007).
[25] A. S. Alexandrov and K. Reynolds, Phys. Rev. B **76**, 132506 (2007).
[26] K. Byczuk, M. Kollar, K. Held, Y.-F. Yang, I. A. Nekrasov, T. Pruschke, and D. Vollhardt, Nature Phys. **3**, 168 (2007).
[27] F. Tan, Y. Wan, and Q.-H. Wang, Phys. Rev. B **76**, 054505 (2007).
[28] M. M. Zemljič, P. Prelovšek, and T. Tohyama, Phys. Rev. Lett. **100**, 036402 (2008).
[29] C. Weber, K. Haule, and G. Kotliar, Phys. Rev. B **78**, 134519 (2008).
[30] B. Moritz, S. Johnston, and T. P. Devereaux, J. Elec. Spec. Rel. Phenom. **181**, 31 (2010).
[31] S. Sakai, Y. Motome, and M. Imada, Phys. Rev. B **82**, 134505 (2010).
[32] F. C. Zhang and T. M. Rice, Phys. Rev. B **37**, 3759 (1988).
[33] P. W. Anderson, Science **235**, 1196 (1987).
[34] E. Dagotto, Rev. Mod. Phys. **66**, 763 (1994).
[35] P. A. Lee, N. Nagaosa, and X.-G. Wen, Rev. Mod. Phys. **78**, 17 (2006).
[36] P. K. Mang, S. Larochelle, A. Mehta, O. P. Vajk, A. S. Erickson, L. Lu, W. J. L. Buyers, A. F. Marshall, K. Prokes, and M. Greven, Phys. Rev. B **70**, 094507 (2004).
[37] N. P. Armitage, F. Ronning, D. H. Lu, C. Kim, A. Damascelli, K. M. Shen, D. L. Feng, H. Eisaki, Z. X. Shen, P. K. Mang, N. Kaneko, M. Greven, Y. Onose, Y. Taguchi, and Y. Tokura, Phys. Rev. Lett. **88**, 257001 (2002).
[38] H. Matsui, T. Takahashi, T. Sato, K. Terashima, H. Ding, T. Uefuji, and K. Yamada, Phys. Rev. B **75**, 224514 (2007).
[39] N. P. Armitage, D. H. Lu, C. Kim, A. Damascelli, K. M. Shen, F. Ronning, D. L. Feng, P. Bogdanov, Z. X. Shen, Y. Onose, Y. Taguchi, Y. Tokura, P. K. Mang, N. Kaneko, and M. Greven, Phys. Rev. Lett. **87**, 147003 (2001).
[40] S. R. Park, Y. S. Roh, Y. K. Yoon, C. S. Leem, J. H. Kim, B. J. Kim, H. Koh, H. Eisaki, N. P. Armitage, and C. Kim,

Phys. Rev. B **75**, 060501 (2007).
[41] E. M. Motoyama, G. Yu, I. M. Vishik, O. P. Vajk, P. K. Mang, and M. Greven, Nature **445**, 186 (2007).
[42] G. Dopf, J. Wagner, P. Dieterich, A. Muramatsu, and W. Hanke, Phys. Rev. Lett. **68**, 2082 (1992).

FIGURES

FIG. 1. (a) Plot of the spectral function intensity along a nodal cut in the first BZ of NCCO ($x = 17\%$) taken at 16.75 eV incident energy. (b) EDCs and (c) MDCs of the cut in (a). The direction of the MDCs and EDCs are indicated by the black arrows in panel (a). The HEA appears as a "waterfall" at an energy scale $\sim 500 - 600$ meV along this cut. Reproduced from Ref. 18.

FIG. 2. Isoenergy surfaces for $x = 4\%$ doped NCCO between E_F (0 eV) and -1.3 eV binding energy. The falsecolor scale has been normalized independently for each isoenergy surface. Surfaces for the first BZ are shown on the left and those for the second BZ appear on the right. The surfaces have been symmetrized along $k_x = 0$ and $k_y = 0$.

FIG. 3. Upper row: High-symmetry cuts in the BZ of $x = 17\%$ doped NCCO. Contours of constant photoelectron intensity (white curves) are included as guides to the eye. The HEA is visible in the nodal cut between $(0, 0)$ and (π, π) (right panel) as a vertical drop with an onset at ~ 0.5 eV. The band bottom at ~ 0.3 eV can be seen in the antinodal cut from $(\pi, 0)$ to (π, π) (middle panel). From the BZ center to $(\pi, 0)$, the isointensity contours suggest a band bottom that persists with little dispersion at ~ 0.5 eV, rising to meet the band bottom in the antinodal region at ~ 0.3 eV. Lower row: EDCs for cuts shown in the upper row.

FIG. 4. Momentum cuts of NCCO ($x = 17\%$) taken at $h\nu$=16.75 eV. (a) Symmetrized FS map with cut directions for panels (b)-(h). (b)-(h) Cuts taken parallel to the crystal a-(b-)axis. Contours of constant photoelectron intensity are added as guides to the eye. (i) EDCs of the respective cuts taken at the BZ axis showing the band bottoms extracted from the cuts in panels (b)-(h).

FIG. 5. Momentum-space cuts of the quantum Monte Carlo simulated electron dispersion for n=1.17 (17% electron doping). The orientation of each cut with respect to the FS is shown in the inset between panels (a) and (b). Details of the simulation method can be found in Refs. 18 and 30 and references therein. There is relatively good, qualitative agreement between the simulated band dispersion and the results shown in Fig. 4 as a function of BZ position. Note the clear "break-up" in the dispersion approaching the BZ axis in panels (d), (e), and (f) similar to the behavior shown in Figs. 4 (f), (g), and (h). Beyond qualitative comparisons, quantitative agreement in energy scales may be achieved with a suitable choice of the energy unit t (*e.g.* $t \sim 400$ meV), the nearest-neighbor, tight-binding hopping parameter that sets the non-interacting band dispersion for the simulation.

FIG. 6. EDCs taken at the momentum space position of the band bottom along the line from $(0, 0)$ to $(\pi/a,0)$ for $x = 4\%$ (a), (b), $x = 11\%$ (c), (d), and $x = 17\%$ (e), (f) doping. Panels (a), (c), and (e) show the band bottom in the first BZ while panels (b), (d), and (f) in the second BZ. The maximum in the EDC second derivative is shown by the filled symbols.

FIG. 7. QMC simulation derived EDCs taken at momentum-space positions along the BZ axis (panels (a), (b), and (c)) and BZ diagonal (panels (d), (e), and (f)) for $n = 1.05(5\%)$ (a, d), $n = 1.15(15\%)$ (b, e), and $n = 1.20(20\%)$ (c, f) electron filling (electron doping).

FIG. 8. Band bottom extracted on the high-symmetry cut from $(\pi/a, 0)$ to $(0, 0)$ by taking the maximum of the EDC second derivative in the first and second BZ, for different dopings. Points are plotted only where the second derivative could yield a maximum. The grey shaded area roughly demarcates where the maximum becomes very broad and weak (cf. fig. 6).

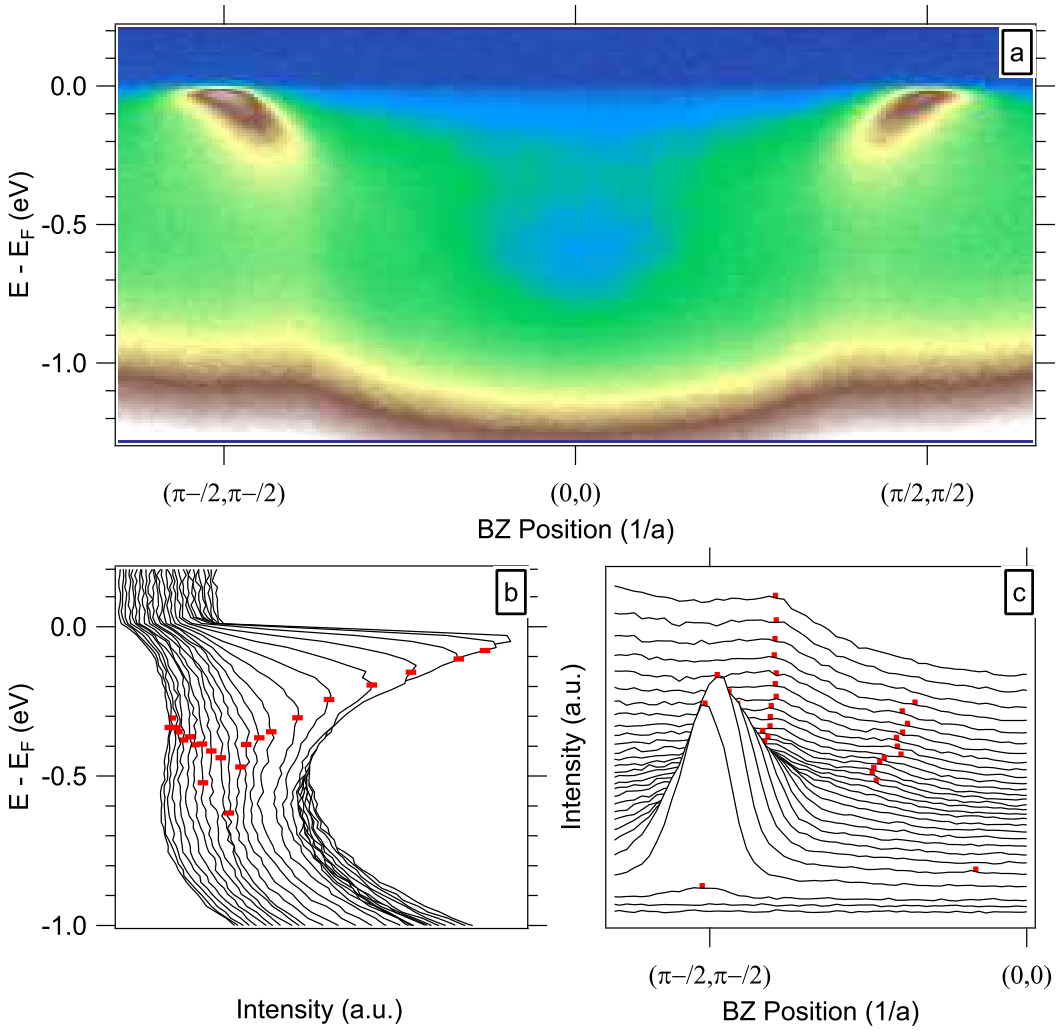

Figure 1 BZ11189 22Feb2011

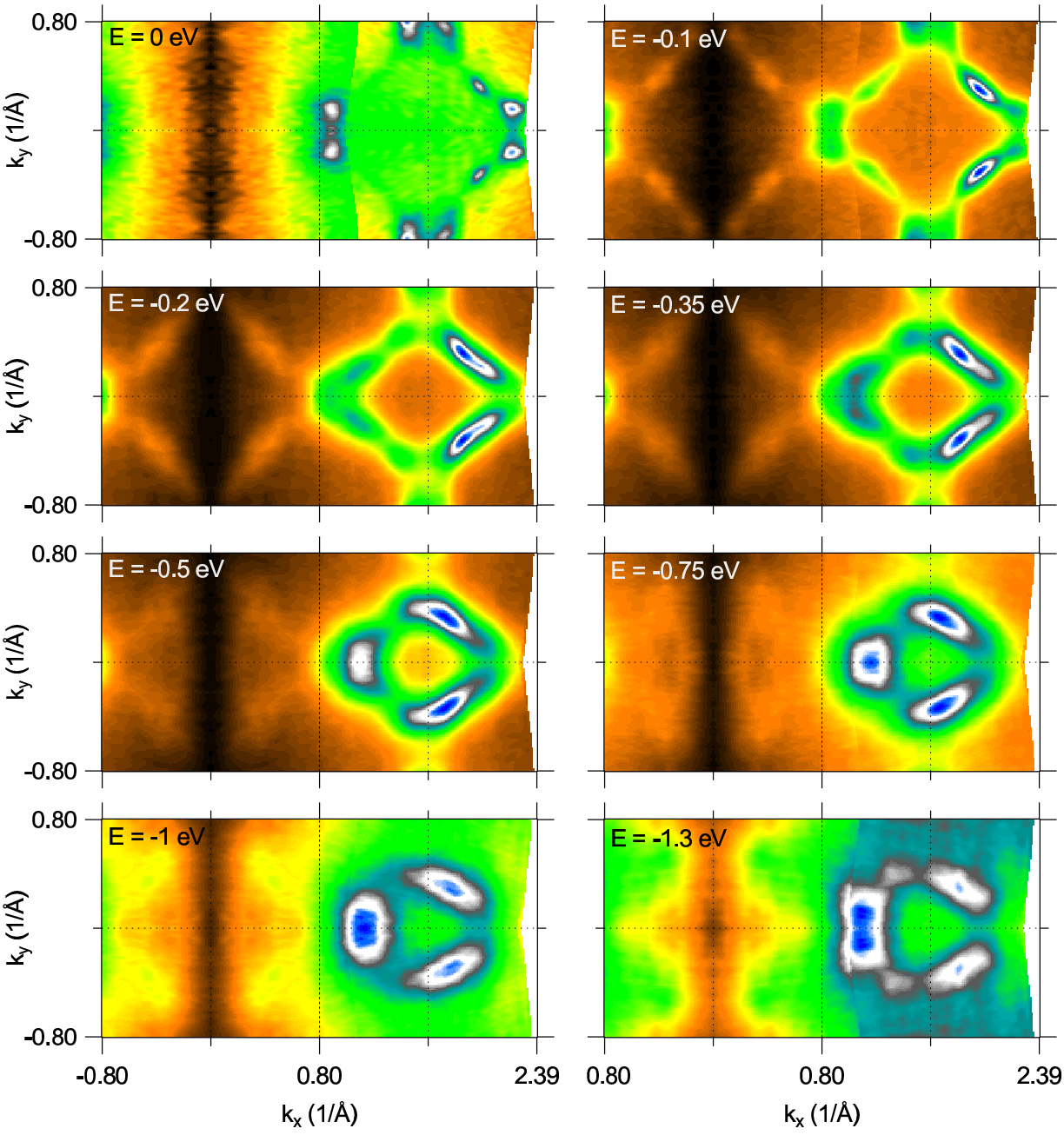

Figure 2 BZ11189 22Feb2011

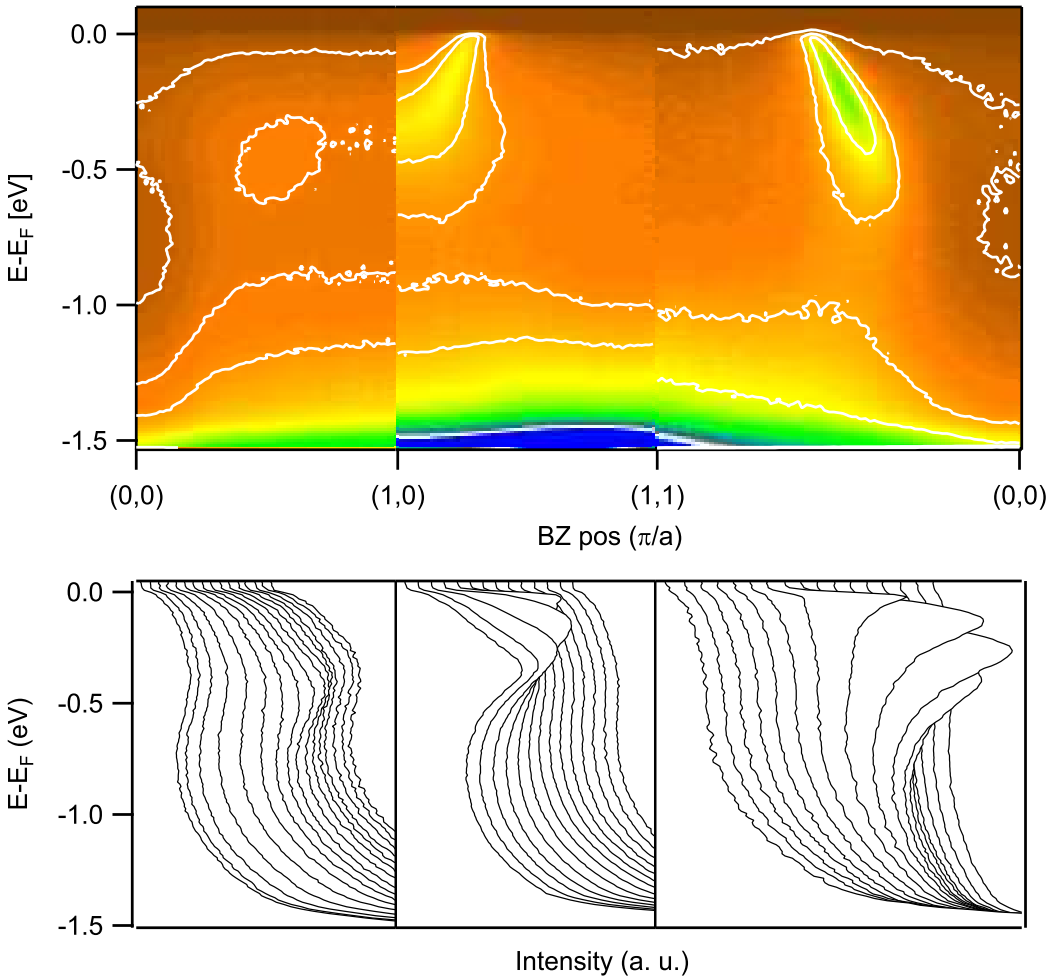

Figure 3 BZ11189 22Feb2011

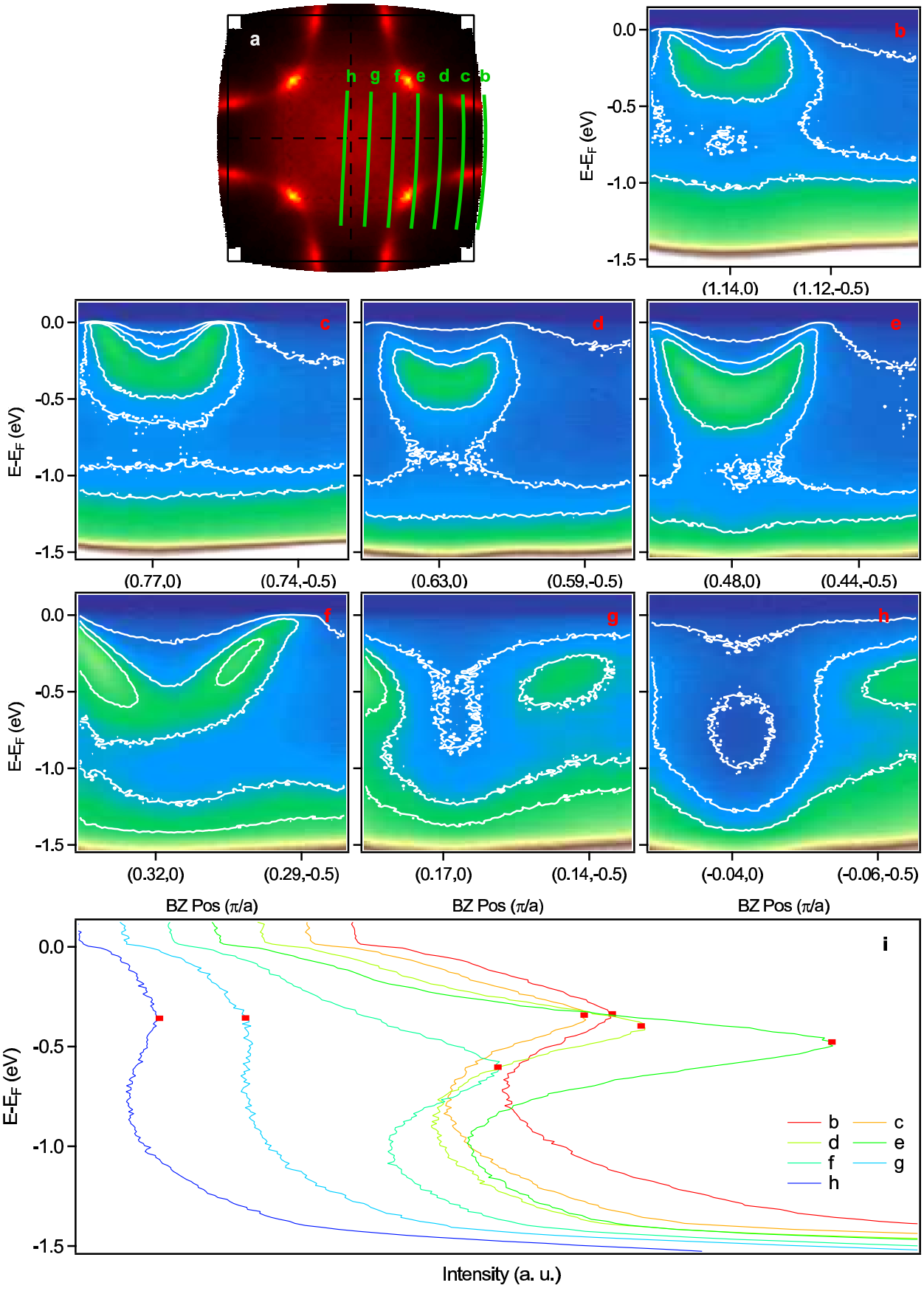

Figure 4 BZ11189 22Feb2011

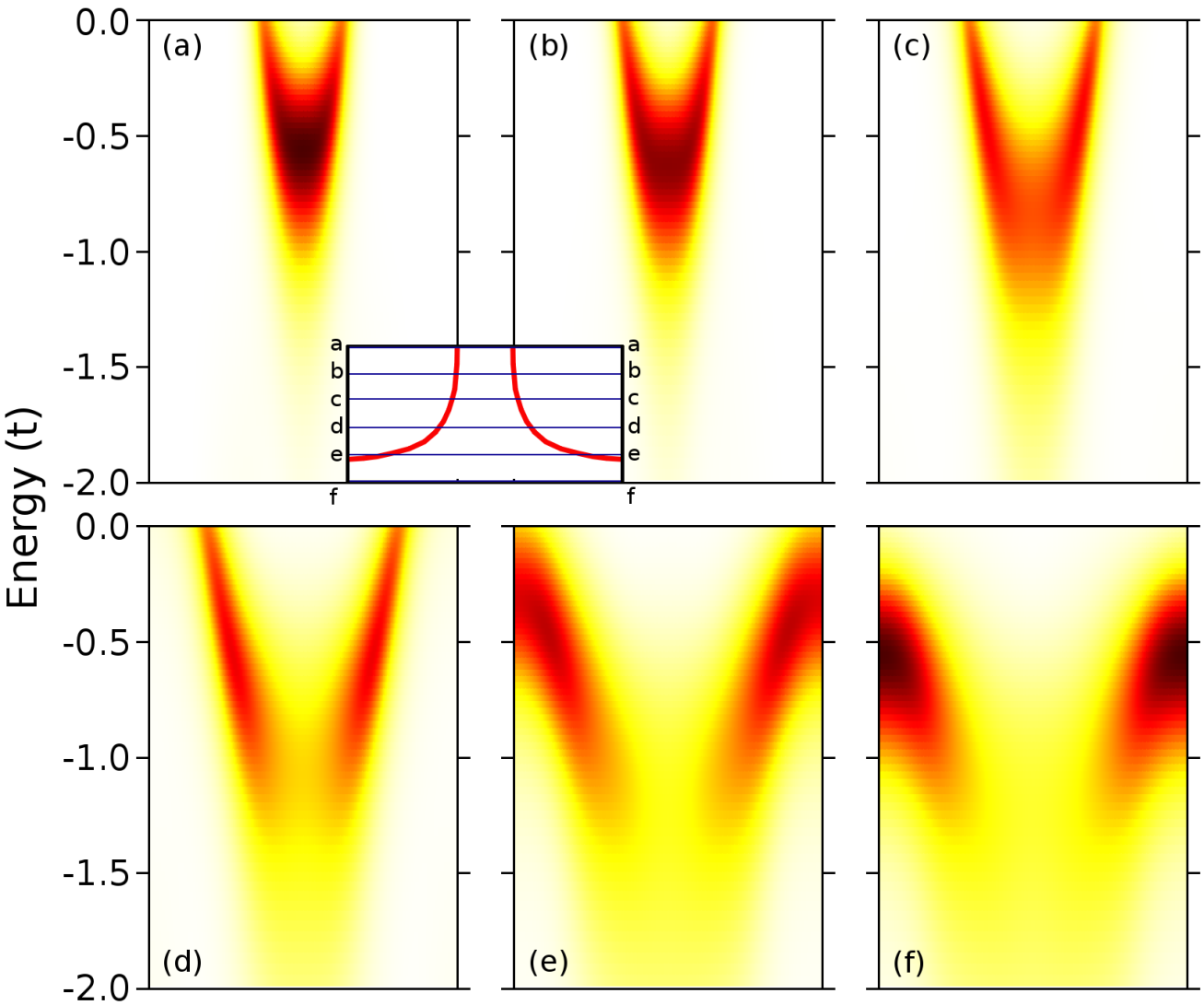

Figure 5 BZ11189 22Feb2011

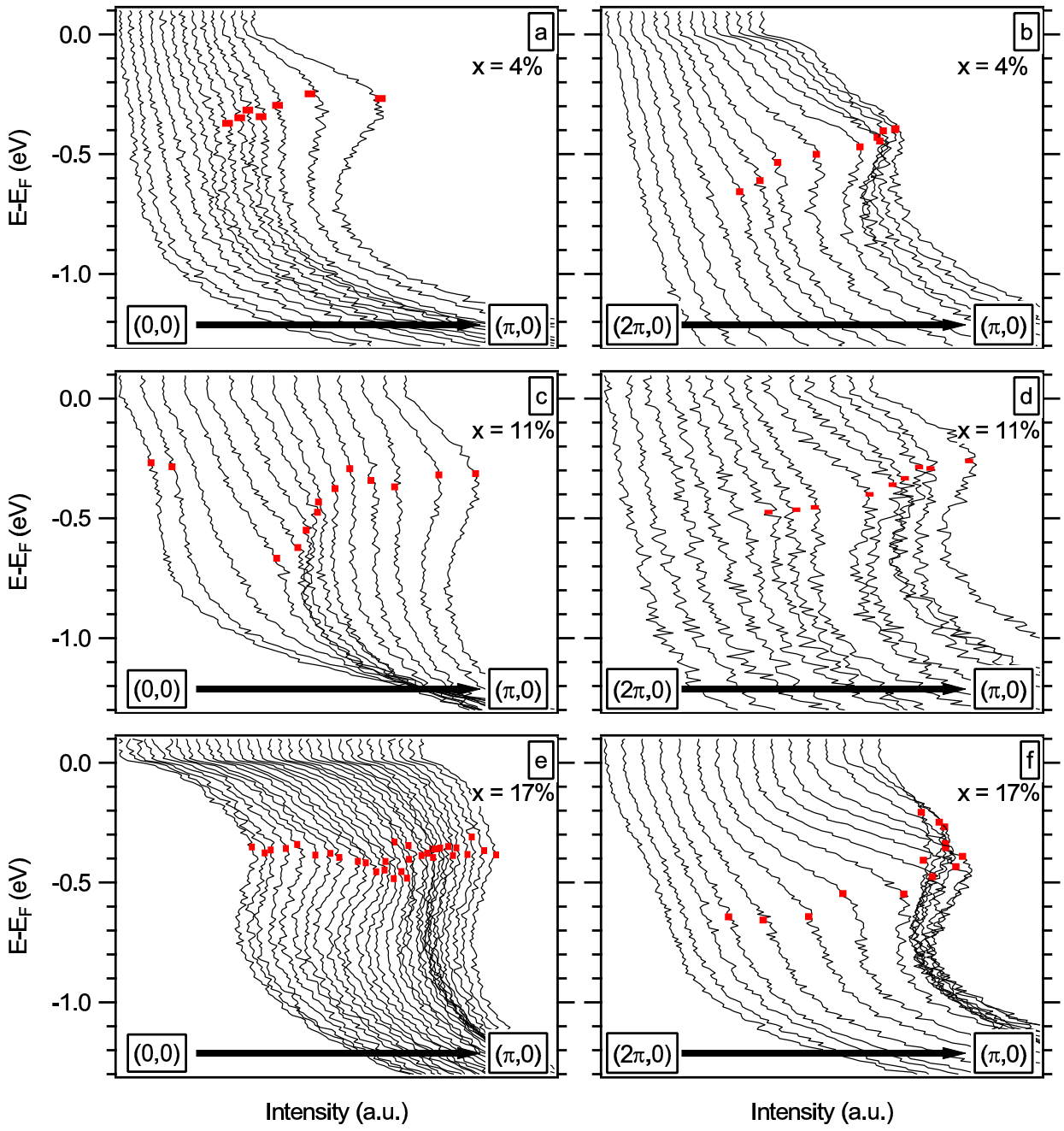

Figure 6 BZ11189 22Feb2011

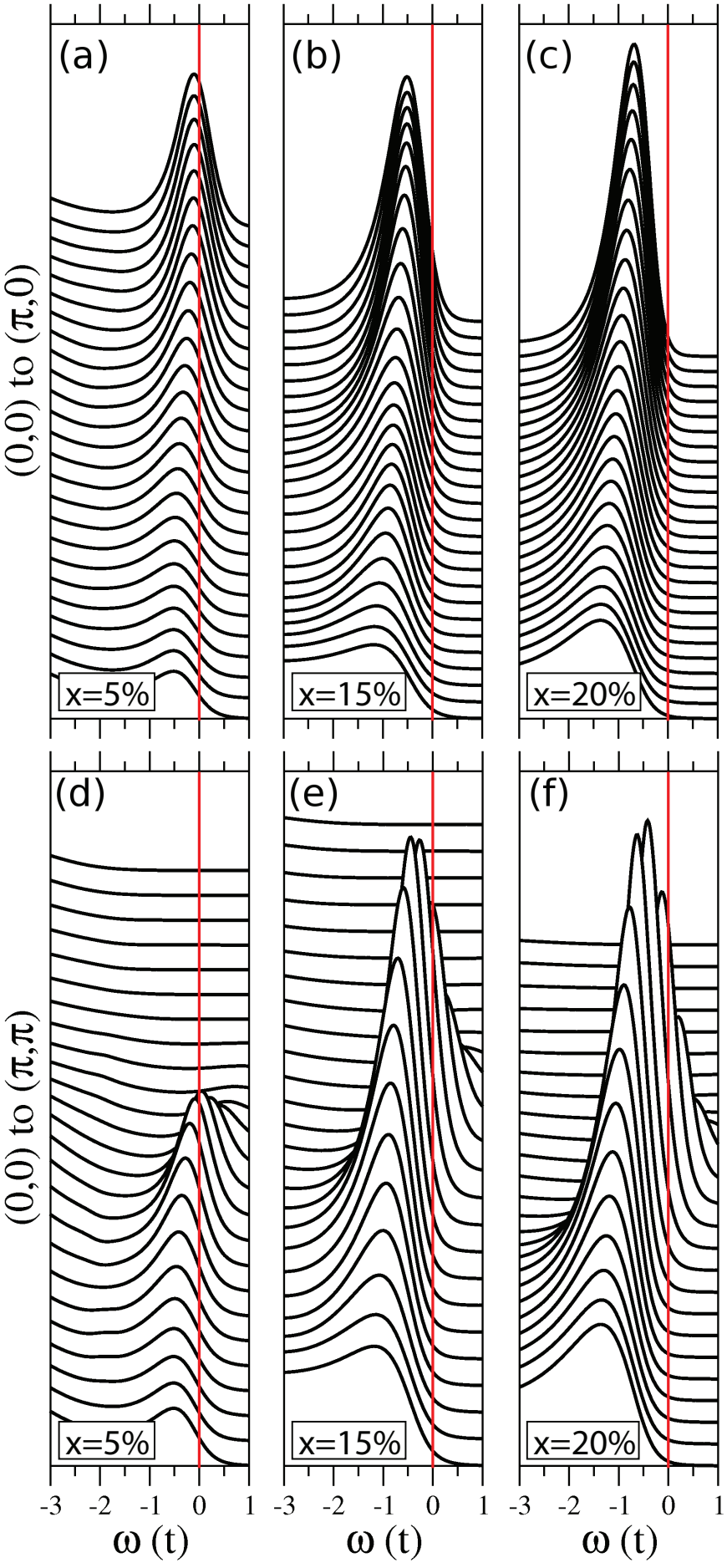

Figure 7 BZ11189 22Feb2011

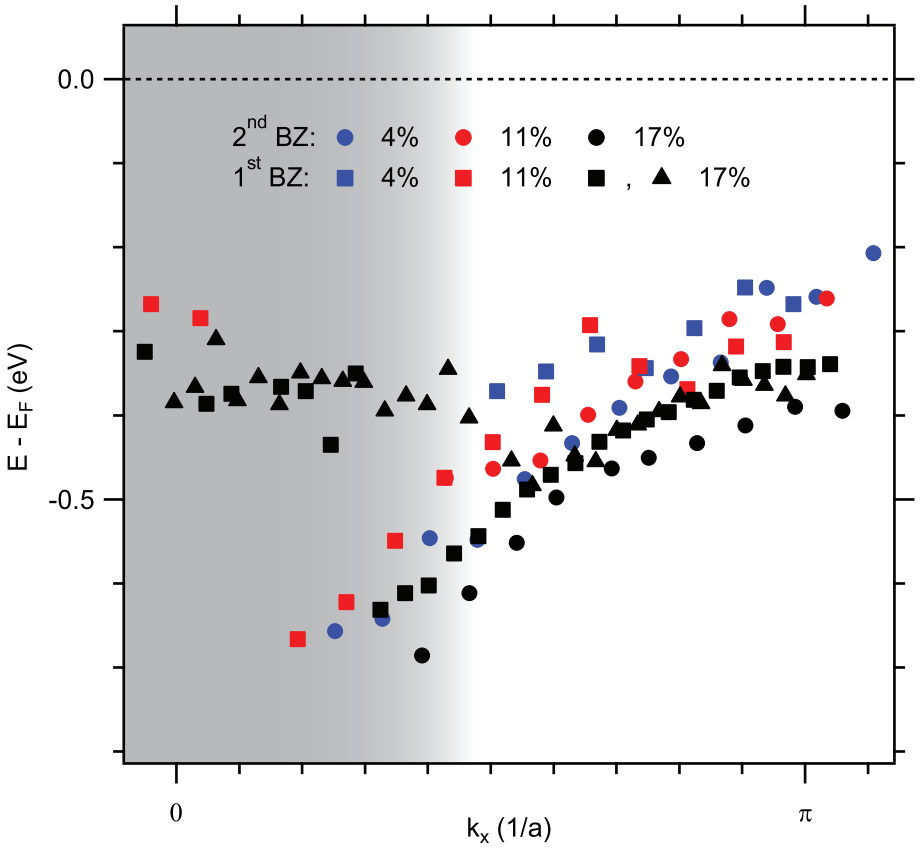

Figure 8 BZ11189 22Feb2011